Force Measurements and Computational Validation of a Transonic Wing-Tip Flow

James R. Grisham,* Michael G. Werling Jr.,† Eric M. Braun,‡ and Frank K. Lu§
University of Texas at Arlington, Arlington, Texas 76019

DOI: 10.2514/1.C033773

A NACA 0012 wing tip was tested at Mach 0.75 and chord Reynolds number of 3 million at incidences from −4 to 7 deg in a transonic Ludwieg tube. The Mach and Reynolds numbers are representative of full-scale rotorcraft blades. Because of the short test time of 0.1 s and high impulse loads, a dynamic calibration was applied to a conventional sidewall force balance to compensate for stress waves propagating within the force balance and test article. Numerical simulations of the entire test section were accomplished to provide data for comparison. The compensated, experimental lift and drag data compared well with the numerical results. This suggests that dynamic calibration improved the experimental data. This comparison demonstrates the feasibility of using complex models for calibrating short-duration wind tunnels in concert with numerical simulation.

I. Introduction

TRANSONIC aerodynamics is critical in a number of applications such as large transport aircraft, fighter aircraft, rotorcraft blades, and turbomachinery. Early studies have revealed discrepancies between pressure and force data obtained in wind tunnels and in flight, these being attributed to wind-tunnel interference and to the difference between flight and test Reynolds numbers. Concerns with these discrepancies continue to this day. To overcome wind-tunnel interference, test sections with porous and slotted walls were successfully introduced, to be followed later by adaptive walls. Despite progress in tackling wall interference, further inroads continue to be made, lately by including independent numerical predictions. Concurrently, there was a realization that "Reynolds number effects" are particularly crucial in the transonic range, and testing should not deviate too far from actual flight conditions. This realization led to the development of pressurized, cryogenic tunnels [1], such as the National Transonic Facility and the European Transonic Wind Tunnel that are able to match the high Reynolds numbers of various flight vehicles. Alternatively, high Reynolds numbers could be achieved using a Ludwieg tube [2] through an unsteady process of exhausting a charge tube filled with high-pressure air. Ludwieg tubes have proven to be versatile aerodynamics and fluid dynamics test facilities and have been developed for testing from subsonic through hypersonic regimes; they continue to remain in use (for example, see [3–9]).

Although large transonic tunnels are industrial workhorses, small-scale university facilities can play a useful role in fundamental aerodynamics research [10]. Among these is a unique, transonic Ludwieg tunnel known as the pilot high-Reynolds-number transonic wind tunnel (HIRT) [11,12]. The HIRT was originally installed at the Arnold Engineering Development Center, Tullahoma, Tennessee, as a 1/13th scale of a larger facility (the actual HIRT), which was never built. Balcazar et al. [13] present a brief history of this facility as well as current operational characteristics.

Ludwieg tubes are short-duration facilities, typically with run times of a few hundred milliseconds. Because of the short run time, there are concerns lately that the dynamic loading of force balances may affect measurements [3]. Development in the understanding of the influence of system dynamics on force measurements has spanned a number of decades, driven primarily by shock-tunnel applications [14]; see [3] for a discussion. It is well known that there are two separate dynamic effects that can affect the dynamic force measurement, namely, the high-frequency stress waves propagating and reflecting in the force balance and test article combination, and the acceleration of the entire facility [15,16]. The location of the load cell or strain gauges also needs to be carefully considered [16].

To mitigate the effects of the aforementioned stress waves, a dynamic calibration is applied to experimental data from a transonic Ludwieg tube. The inspiration for this work comes from force measurement methods in hypersonic shock tunnels [17]. According to Juhany and Darji, the test time of approximately 100 ms is of sufficient duration to obviate the need for acceleration compensation unlike the even shorter-duration hypersonic shock tunnels [3].

An encouraging development in aerodynamics testing is the synergistic use of computational fluid dynamics (CFD) and finite element analysis throughout the different phases of a test campaign. These include force balance and test article design, prediction of the aerodynamics, and subsequent comparison with experimental data. Although the conventional perspective is to provide experimental data to validate and verify CFD results, the converse in using CFD for determining wind-tunnel conditions such as flow angularity as well as wall and mounting interference is also important [18]. Gardner and Richter [19] highlighted the difficulties of a purely experimental approach for sorting out the various contributions to experimental uncertainty and proposed that high-fidelity numerical simulations can assist in interpreting experimental data and can also identify areas of concern. Thus, the flowfield details afforded by CFD are helpful in providing more information to the analyst, which in turn allows for a better interpretation of the relevant physical phenomena, provided that the tools have been properly verified and validated [20].

The purpose of this paper is to evaluate the effectiveness of using a dynamic calibration to remove artifacts that arise from stress waves propagating through the structure of the wind tunnel and the balance itself. This task is accomplished by comparing uncompensated and compensated experimental results with results from other studies as well as independent numerical simulations of the entire test section. The comparison shows that accounting for the dynamics of the facility yields better agreement with the computational results as well as results from previous studies. It will be shown that the dynamic

Received 18 October 2015; revision received 13 January 2016; accepted for publication 3 February 2016; published online 4 May 2016.

*Graduate Research Associate, Aerodynamics Research Center, CFD Laboratory, Department of Mechanical and Aerospace Engineering. Student Member AIAA.

†Graduate Research Assistant, Aerodynamics Research Center, Department of Mechanical and Aerospace Engineering; currently Engineer, Solar Turbine, New Orleans, LA 70123. Member AIAA.

‡Graduate Research Associate, Aerodynamics Research Center, Department of Mechanical and Aerospace Engineering; currently Test and Evaluation Engineer, The Boeing Company, Huntsville, AL 35808. Senior Member AIAA.

§Director, Aerodynamics Research Center, Department of Mechanical and Aerospace Engineering. Associate Fellow AIAA.

calibration procedure improves the reliability of Ludwieg tubes in obtaining aerodynamic data.

II. Experimental Method

A. Test Facility and Operation

The HIRT, shown schematically in Fig. 1, has general features that are similar to the more familiar supersonic blowdown tunnel, possessing a nozzle to raise the Mach number to the desired value as well as a test section and a diffuser. The major components of this particular facility include a 33.8-m-long (111-ft-long) charge tube with an internal diameter of 353 mm (14 in.). The charge tube is connected to a nozzle with an area contraction ratio of 2.27. This constant ratio typically requires a minimum charge pressure of about 520 kPa (75 psia) to produce a minimum flow velocity in the test section. The nozzle also transitions the circular cross section of the charge tube to a rectangular one for the test section. The Mach number is obtained through moving a combination of ejector flaps and valves that will be briefly described later.

The test section is 18.5 cm high by 23.2 cm wide and is nominally 60–64.5 cm long ($7.28 \times 9.13 \times 23.62 - 25.4$ in.). The length is 60 cm if all four porous walls are installed. The test section can be surrounded by four porous sides, or have only porous top and bottom, or completely solid side walls. Immediately downstream of the test section is a set of ejector flaps that, when opened, enable the flow in the test section to become supersonic. Next follows the diffuser, which transitions the cross section from rectangular back to circular. Mounting for models or probes is provided in the diffuser section.

As is typical of transonic tunnels with porous walls, air is vented through these walls to ensure that shocks that impinge upon these surfaces do not reflect back onto the test article or its mount that will seriously distort the flow from that without walls. A plenum cavity surrounding the test section allows it to be vented. Flex hoses connect the plenum shell to a manifold to vent the plenum cavity. Within the manifold is the diaphragm holder, made of two plates that are used to clamp one or more diaphragms made of Mylar film. The diaphragms seal the entire Ludwieg tunnel from the ambient, thus allowing the pressure to build when filling the tube.

The Ludwieg tunnel is started by computer-controlled actuation of the sliding sleeve valve (SSV) and a cross-shaped cutter to rupture the diaphragm in the plenum exhaust line. The number of open ports on the SSV, the ejector flap position, and the plenum exhaust cross-section area can be varied to control the mass flow rate and thereby the test-section Mach number. The opening process creates an expansion wave that moves from the diffuser through the test section, the nozzle, and into the charge tube. A wave diagram of the ideal, unsteady process is shown in Fig. 2. The unsteady expansion reflects off the head of the charge tube and travels downstream. A period of quasi-steady flow is established in the test section between the two wave systems as shown in the figure. For this particular Ludwieg tunnel, the test time is 80–120 ms. Refer to [13] for a more detailed explanation of the HIRT starting process and functionality of the components labeled in Fig. 1. The maximum pressure of the charge tube is 5.15 MPa (750 psia), which produces a stagnation pressure of 3.45 MPa (500 psia) and Reynolds numbers of up to 400 million/m (120 million/ft).

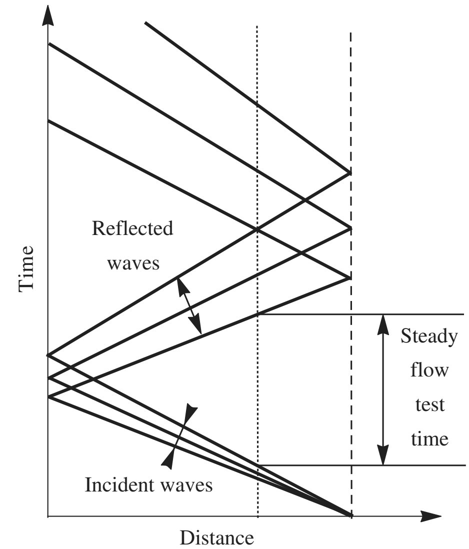

Fig. 2 Wave diagram showing the ideal, unsteady expansion propagation within the Ludwieg tube.

B. Data Acquisition

Previous operation of the Ludwieg tunnel showed that the test-section flow is uniform [11,21–23]. The previous studies also showed that the test conditions are highly repeatable, and these observations were also found to be true in the present investigation.

National Instruments (NI) equipment was used to read the pressure, temperature, and force balance signals with simultaneous sample-and-hold data-acquisition systems. The raw data were subsequently reduced to obtain the Mach and Reynolds number and aerodynamic parameters such as forces and moments, as necessary. A total pressure transducer was mounted in the charge tube, whereas the static pressure transducer was mounted flush with the ceiling in the test section. There are also static pressure transducers behind each side wall to measure the plenum static pressure. A type K thermocouple, also located in the charge tube, was used to measure the total temperature. The axial and normal force data were acquired by strain gauge modules, each with a lowpass filter at 1.6 kHz. The data were digitized by an NI data acquisition card with 12 bit resolution and a maximum sampling rate of 200 kS/s. All control and data-acquisition functions were executed through an in-house NI LabVIEW program, which allowed the sampling rate and sample time to be easily changed and which set the delay times between the SSV and the diaphragm cutter. Further details can be found in [24].

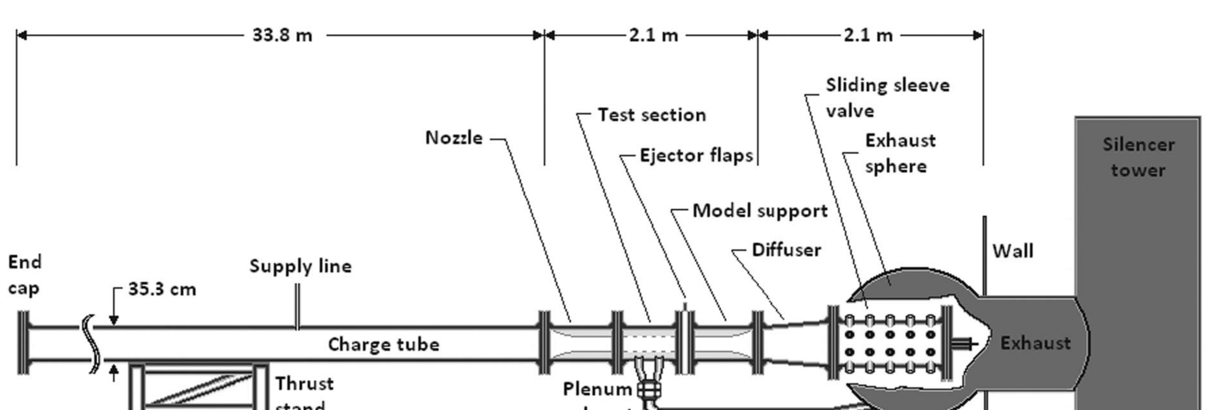

Fig. 1 Ludwieg tube schematic.

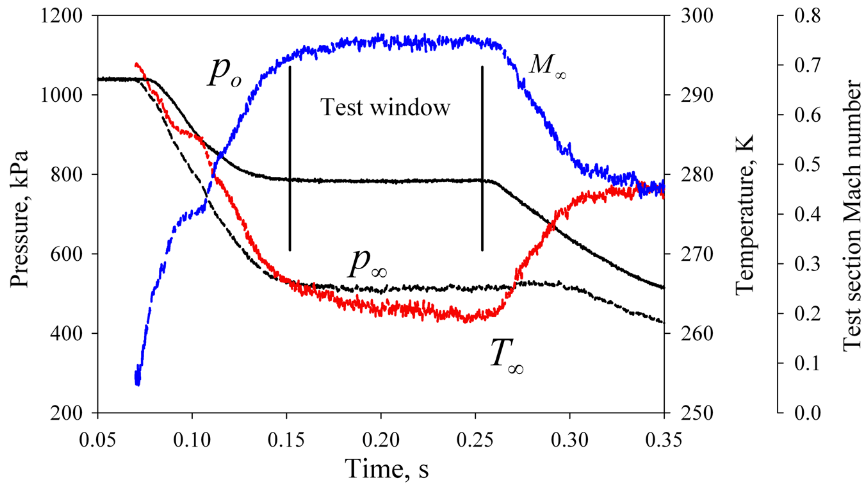

Fig. 3 Example data of the total pressure and local temperature during a test run.

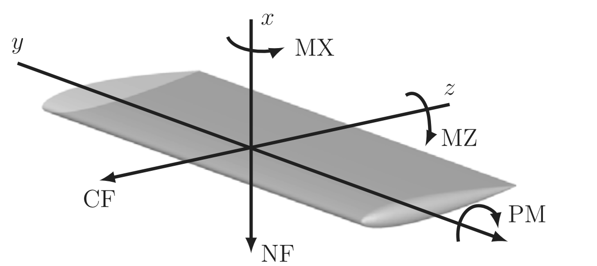

Fig. 4 Schematic of the measured forces and moments on a model by the sidewall force balance.

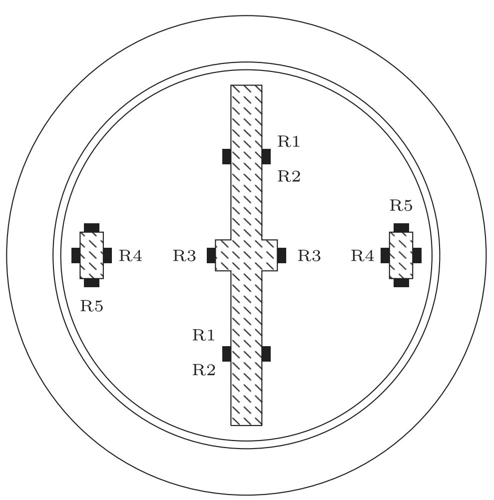

Fig. 5 Strain gauge layout.

An example of the pertinent pressure and temperature data is shown in Fig. 3, together with the calculated Mach number. The quasi-steady flow test window of about 0.1 s is indicated in the figure.

The nominal, chord Reynolds number was 3 million to an uncertainty of 1–2% per run, and the Mach number was 0.75 ± 0.015. Run-to-run variations of Reynolds number were less than 4%.

It can be noted that all the parameters were functions of time. Further statistical analyses were performed within the quasi-steady time window of 0.1 s to obtain mean values that were quoted previously. The standard deviations within this time window were also computed and were used as a measure of data uncertainty.

C. Force Measurement

A conventional, five-component, sidewall balance with internal strain gauges was used to measure the normal force (NF), the chord force (CF), the rolling moment (MX), the yawing moment (MZ), and the pitching moment (PM), as shown schematically in Fig. 4. Details on the force balance and its operation can be found in [24], and only a summary is provided here. The forces and moments were picked up by pairs of strain gauges labeled R1–R5, as shown in the schematic of Fig. 5. As listed in Table 1, the normal force and rolling moment required a combination of strain gauge readings, whereas the other components were picked up by individual gauges. The maximum loading value for each component is also given in the table. These values are large to accommodate the high dynamic pressure of the facility.

In the reported experiments, the pitching axis of the balance was located at the quarter-chord of the test article, which was a semispan wing model with a NACA 0012 and rounded at its tip. The test article is shown attached to the force balance in Fig. 6. The wing-tip model had a chord of 51 mm (2.0 in.), a span of 109.2 mm (4.3 in.), and a planform area of 5571 mm^2 (8.635 in^2). The lift and drag coefficients were obtained from the measured normal and chord forces.

1. *Static Calibration*

The raw strain gauge data θ were combined with the sensitivity constants S to obtain the forces and moments, with these written as elements of a vector $\boldsymbol{F}^{[0]}$ and the relationship given by

$$\boldsymbol{F}^{[0]} = [\theta_{\mathrm{NF}}\ \theta_{\mathrm{MX}}\ \theta_{\mathrm{CF}}\ \theta_{\mathrm{MZ}}\ \theta_{\mathrm{PM}}][S_{\mathrm{NF}}\ S_{\mathrm{MX}}\ S_{\mathrm{CF}}\ S_{\mathrm{MZ}}\ S_{\mathrm{PM}}]^T \qquad (1)$$

The calibration jig shown in Fig. 7 allowed for calibration of one or two components at a time, following conventional procedure [25–27], the details of which can be found in [24]. The pin A in the center of the jig was used for calibrating the normal force or the chord force, depending on the axis, without creating moments. The holes labeled B or C on the centerline were 25.4 and 50.8 mm (1 and 2 in.), respectively, from the center, which allowed for moments to be applied. The holes labeled D and E on each arm were used to create the pitching moment. All of these holes were threaded to accept the pin that is located at A in the figure.

Instead of the test article, the calibration jig was fastened to the force balance, the back end of which was in turn clamped tightly to a

Table 1 Components found from strain gauge combinations and their maxima

Component	Related bridge	Maximum load
Normal force, NF	R1 − R2	1830 N (500 lbf)
Rolling moment, MX	R1 + R2	113 N · m (1000 lbf in.)
Chord force, CF	R3	275 N (75 lbf)
Yawing moment, MZ	R4	17 N · m (150 lbf in.)
Pitching moment, PM	R5	16 N · m (140 lbf in.)

Fig. 6 Force balance with the NACA 0012 wing tip.

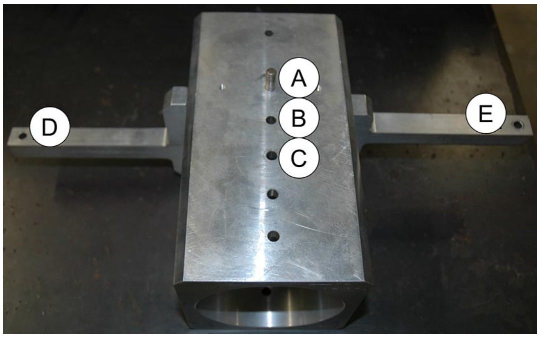

Fig. 7 Static calibration jig with loading points labeled.

work table via an aluminum stand. The jig hung over the edge of the table, directly above a base plate. The arrangement is shown in Fig. 8. The base plate was firmly attached to the floor directly below the force balance. A digital scale with a 2.2 N (0.5 lbf) resolution was attached to one of the eyebolts on the base plate and to the force balance by a chain and a turnbuckle. Such a setup allowed for static loads of up to 2.2 kN (500 lbf) to be applied without the need for large standard weights.

The calibration procedure consisted of taking strain gauge readings by the data-acquisition system for each load increment, starting with the tare reading. The loads were applied in approximately equal increments up to the maximum value allowed by the strain gauge or the instrumentation. Five-point calibrations for the normal and chord force and the pitching moment components were linear, yielding their respective sensitivity coefficients S, with the majority of the correlation coefficients exceeding 0.991.

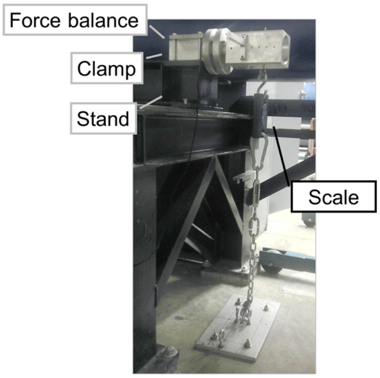

Fig. 8 Static calibration setup for the normal force component.

As described in [25–27], the calibration procedure is a complex but well-understood procedure that arrives at a set of balance interaction equations. The raw strain gauge data can be affected by misalignments in the balance and from the elastic deformations, the latter of which could be nonlinear. The combination of these effects means that the strain gauge data are affected by mutual interactions between the forces and moments. Modern practice is to build a balance matrix $\boldsymbol{M}$ to account for these interactions, which in the present case is a 5×13 matrix [24].

2. *Dynamic Calibration*

The impulsive start of the Ludwieg tube sets up stress waves throughout the facility that would not have damped out by the end of the test period. These stress waves interfere with the load measurement in a complex manner. Thus, in addition to static calibration, dynamic calibration is needed due to the short run times. Dynamic calibration is well developed for hypersonic shock tunnels with even shorter run times of $\mathcal{O}(0.1\text{–}1)$ ms [14], with many recent advancements [28]. In addition, force measurements in shock tunnels may require acceleration compensation due to the run time being of the same order as the characteristic time for stress waves propagating and reflecting in the facility [15].

For the present Ludwieg tunnel, there is no need to consider acceleration compensation. This conclusion was reached by Juhany and Darji [3], who tested a sting-mounted force balance in a similar facility. However, a dynamic calibration is still needed to remove the dynamics associated with stress waves propagating within the force balance. These stress waves travel at characteristic times that are of the order of the quasi-steady test time and would appear to result in extraneous inertia forces. Knowing the dynamics of the balance and model allows the history of the forces that are applied to be determined from the raw measurements using an approach developed in shock tunnels [17].

The model and the balance can be considered to be a linear, time-invariant system. Following Mee [17], if the output of the system is $y(t)$, which includes the developed interference within the model, and the applied load is $x(t)$, then the input and output can be related via convolution:

$$y(t) = h(t) * x(t) = \int_0^t h(t-\tau)x(\tau)\,\mathrm{d}\tau \tag{2}$$

where $h(t)$ is the impulse response function. Different methods can be used to determine $h(t)$. For this calibration, a known impulse input $x(t)$ is applied to the balance and model while measuring the corresponding output $y(t)$. Manipulating the Fourier transform of Eq. (2) yields the transfer function

$$H(f) = \frac{Y(f)}{X(f)} \tag{3}$$

where $Y(f)$ and $X(f)$ are the transforms of $y(t)$ and $x(t)$, respectively. The transfer function $H(f)$ is assumed constant between the calibration and during testing. This assumption is valid because the test article remains fixed to the force balance, the calibration rig and the Ludwieg tunnel can be considered to be rigid, and the bridge circuit settings are not changed. Therefore, the transfer function is independent of the input. The inverse Fourier transform is then applied to $X(f)$ to yield the true input on the model and balance $x(t)$, the desired outcome.

The test setup is similar to that of the static calibration setup discussed previously. The test article was attached to the force balance instead of the static calibration apparatus. An instrumented PCB impact hammer with a rubber tip was used to excite the strain bridges within the balance. The rubber tip prevents damage to the model and balance. The impulse was directed in the same direction as the force that was measured by the bridges. For example, the hammer

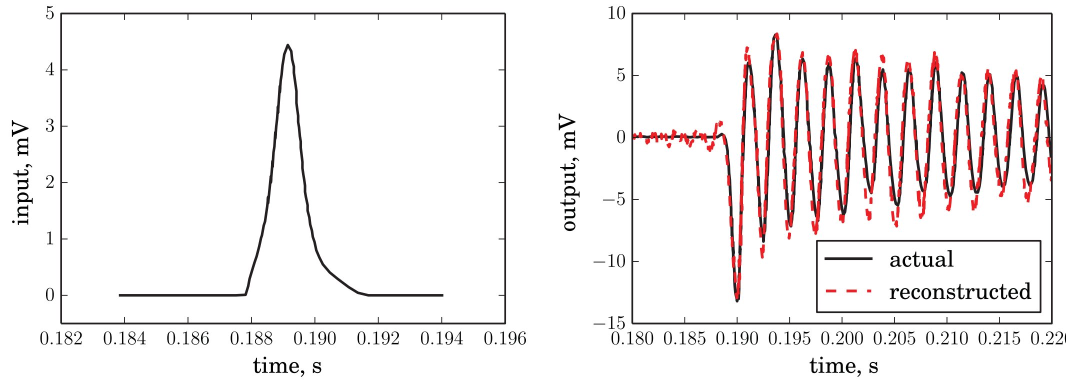

a) Input signal **b) Actual and reconstructed output signals**

Fig. 9 Example input and output data for dynamic calibration.

struck either the leading edge or the trailing edge of the wing tip for the chord force as well as the top or bottom surface of the wing tip for the normal force. A high sampling rate of 50 kS/s was employed to be able to capture the stress waves with wave speed of approximately 5190 m/s [29].

A common issue associated with digital deconvolution is numerical instability due to the presence of high frequencies. If the initial value of the physical response is close to zero, and because dividing by low values is in fact a large multiplier, noise and error can be greatly magnified. Because of this, instability occurs because each input sample is dependent on the previous value [30]. Stability of the deconvolution was accomplished by reducing noise, removing outliers, and filtering.

An example of the input measured by a load cell on the instrumented hammer is shown in Fig. 9a, and the corresponding output is shown in Fig. 9b by the curve labeled "actual." Once the transfer function is obtained, it was checked by generating the curve labeled "reconstructed," which was obtained by convolution of the input with the impulse response function. It can be seen that the regenerated signal agrees well with the actual signal. The transfer function is selected from a number of dynamic calibrations only when there is such good agreement.

After the transfer functions were determined for the NF and CF components, the force balance and wing model were attached to the Ludwieg tunnel, as shown in Fig. 10. Tests with the angle of attack α from -4 to 7 deg were conducted at $M_\infty = 0.75 \pm 0.015$, $Re_\infty = 3$ million $\pm 1 - 2\%$, and $q_\infty = 204.1$ kPa. A discussion of the results follows the discussion on the numerical method.

III. Numerical Method

NASA's FUN3D flow solver was used to numerically solve the Navier–Stokes equations for the entire test section with the wing tip set at angles of attack ranging from -3 to 4 deg [31]. The turbulence model used was that of Spalart and Allmaras. Feature-based refinement along with a mesh study was used to ensure a mesh-independent solution. The wall y^+ was set to unity using the typical correlations for skin friction. The flow solver is second-order accurate in space and uses local time stepping for the steady simulations presented in this paper. The simulations made use of Roe flux difference splitting. No flux limiter was used.

Fig. 10 View upstream of Ludwieg tube showing the wall-mounted wing tip.

Flow across the porous walls can be modeled using the difference in pressure between the test section and the plenum [32]. The difference in pressure can be expressed as

$$\Delta C_p \equiv \frac{p_\infty - p_{\text{plenum}}}{(1/2)\rho u_\infty^2} \tag{4}$$

For the current experiments, $\Delta C_p \approx -0.04$, which is relatively small. For this reason, the porous walls were not modeled in the present work (that is, they were set to no-slip walls).

The meshes were generated using Pointwise and AFLR3 [33,34]. Specifically, a script was written to generate the geometry and surface meshes in Pointwise. The surface mesh was then input to AFLR3 for volume mesh generation. Figure 11a shows the test-section geometry that was modeled; the upper, lower, and closest walls are not shown for clarity. The dimensions of the geometry shown next are identical to the actual test-section dimensions. The walls and the wing were modeled as no-slip walls. Figure 11b shows the mesh on the upper surface of the wing, which consisted of approximately 86,000 cells. The original meshes (i.e., before adaptation) consisted of approximately 6.3 million nodes and 37 million tetrahedral cells. The mesh was frozen below $y^+ \approx 300$ so that boundary-layer resolution was maintained throughout the adaptation process.

The feature-based mesh-adaptation process involved two main steps, namely, computation of a metric that represents the desired cell size and adaptation of the mesh to achieve the desired result. In this work, the flowfield variable used to compute the metric was the Mach number. A Hessian matrix was then formed using a least-squares gradient calculation. This Hessian matrix was used to stretch the mesh, and the scalar flowfield variable was used to determine the isotropic spacing. For more details, see [35,36]. Some sample results of the adaptation applied to this configuration can be seen in Fig. 12. The mesh adaptation improved the residual convergence of the flow solver while also decreasing the number of grid points by roughly 27%, down to approximately 4.5 million nodes and 27 million tetrahedral cells.

IV. Results and Discussion

Figure 13 shows a comparison between the numerical, compensated experimental data, uncompensated experimental data, and two-dimensional data from Mineck and Hartwich [37] and Harris [38]. The results follow the expected linear trend in C_L with angle of attack.

The studies by Mineck and Hartwich [37] and Harris [38] involved only positive incidences. Mineck and Hartwich's data [37] were obtained at $M_\infty = 0.76$ and a chord Reynolds number of 4 million. The data were obtained close to present conditions and show general trends. Mineck and Hartwich mentioned that the upper surface shape of their model deviated slightly from the actual one. They also thought that there may be a model misalignment of -0.1 deg due to either flow angularity or the actual model attitude when comparing their data with [38]. The figure shows that the two-dimensional lift

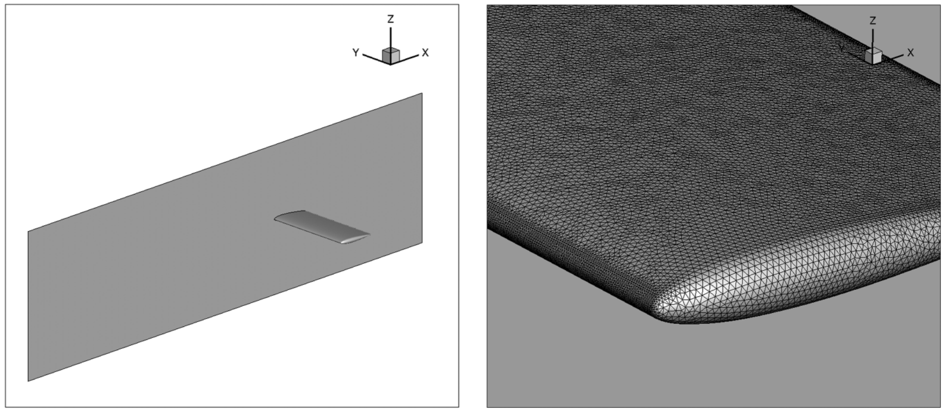

a) Geometry b) Surface mesh on the wing

Fig. 11 Geometry and surface mesh.

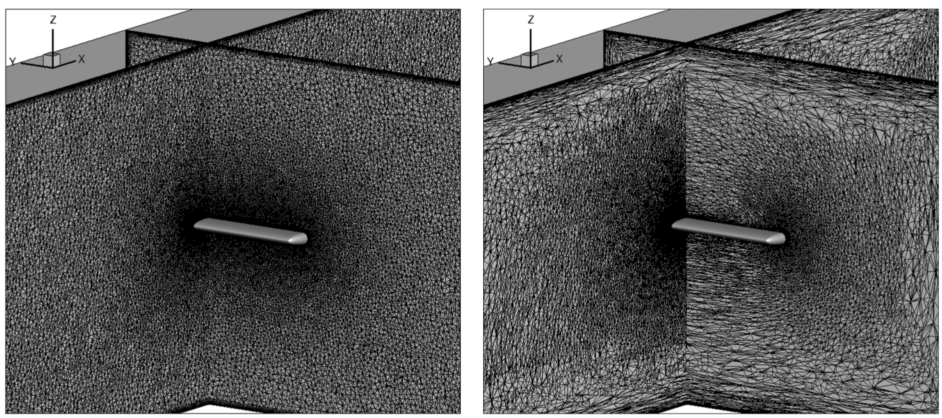

a) Original b) Adapted

Fig. 12 Comparison between original and adapted meshes.

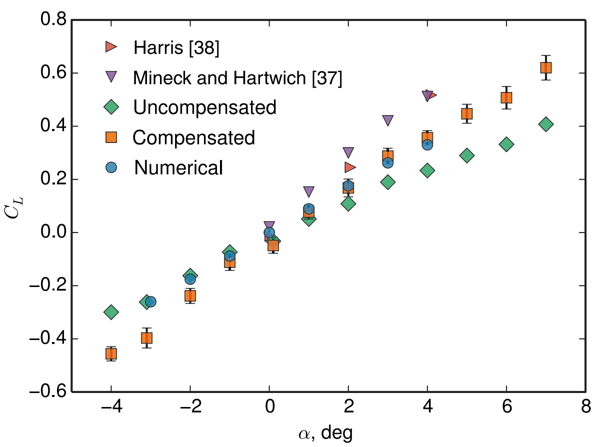

Fig. 13 Lift coefficients of NACA 0012 wing tip at Mach 0.75.

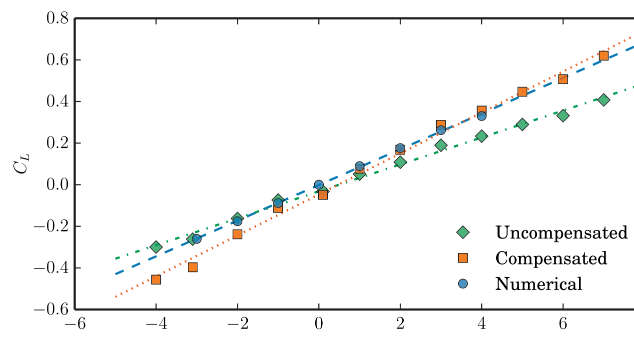

Fig. 14 Comparison between slopes of C_L vs α curves.

curve slope is higher than that of the present finite wing. This is to be expected because the finite wing reduces the effective angle of attack. For the present discussion, the interest lies not in a detailed comparison with two-dimensional data but to ensure that the proper trends are observed and that CFD can be used to help with understanding the experimental data.

A close examination of Fig. 13 for positive angles of attack reveals that the dynamic calibration vastly improves the agreement between CFD and the experiment. This is opposite for negative angles of attack. That is, at negative angles of attack, the uncompensated data agree with the numerical results better than the compensated data.

To further explore this discrepancy, a linear regression was computed for each of the data sets (see Fig. 14). The slopes for the numerical, uncalibrated, and calibrated (per degree) are 0.0858, 0.0647, and 0.0985, respectively. Applying the calibration moves the slope of the C_L vs α curve closer to the value obtained using CFD. The percentage difference between the experimental data sets and CFD data was computed. For the uncompensated case, the slope is 24.5% less than the result obtained from CFD and is 14.8% more for the compensated case. This result shows that, although there are some discrepancies at negative vs positive angles of attack, the dynamic calibration improves the trends.

Figure 15 shows a comparison between the drag polars. The positive effects of the dynamic calibration are most evident in this figure. Application of the dynamic calibration causes the experimental data to be shifted down, closer to the numerical data and that of the two-dimensional wings. Another important piece of information can be gleaned from the plot. The wing tip is made up of a symmetric airfoil, the NACA 0012. Because of this, the drag polars

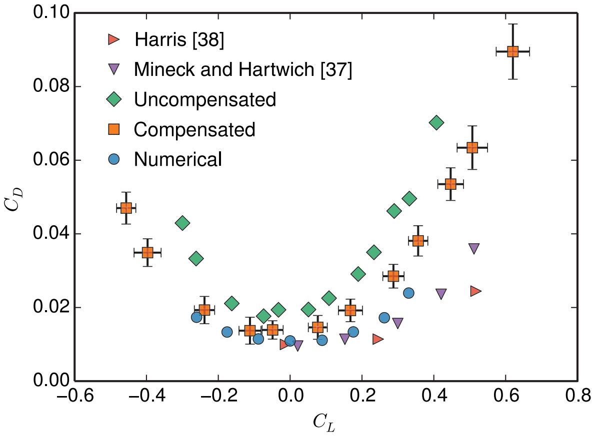

Fig. 15 Drag polar of NACA 0012 wing tip at Mach 0.75.

should be symmetric about $C_L = 0$. Examination of the figure shows that this is not true for the compensated and uncompensated experimental data. The lack of symmetry points back to the possibility of model misalignment, some angularity in the tunnel, or machining imperfections. This is a topic for further investigation.

Regardless of the discrepancies described previously, the comparisons illustrate the effectiveness of the dynamic calibration. As mentioned in the previous paragraph, the mismatch is most likely due to flow angularity, model misalignment, or manufacturing issues, not the dynamic calibration, which is the novel part of the present work. The dynamic calibration brought the experimental data closer to the numerical data, thereby reducing uncertainty.

V. Conclusions

A unique set of lift and drag data for a NACA 0012 wing tip were obtained in a transonic Ludwieg tube. A dynamic calibration was applied to the force balance to account for impulsive loading associated with the short run times of Ludwieg tubes. Numerical solutions of the entire test section at several angles of attack were undertaken to provide data for comparison. Comparing the data from the present experiments, numerical solutions and other two-dimensional airfoil experiments reveal the effectiveness of the dynamic calibration. In general, the compensated experimental data are shown to be in better agreement with the numerical and two-dimensional results than the uncompensated data. Some small discrepancies at negative angles of attack are present and are believed to be due to the flow angularity, model misalignment, and/or manufacturing errors, not the dynamic calibration. This comparison demonstrates the feasibility of using complex models for calibrating wind tunnels in concert with numerical simulation. The major finding of this work is that the dynamic calibration described herein is capable of accounting for and removing artifacts due to the propagation of stress waves through the wind tunnel and force balance.

Acknowledgments

The authors would like to thank the FUN3D team for answering questions about operating the code as well as Pointwise and the SimCenter at Mississippi State University for the use of their meshing software. The computations were performed using high-performance computing resources at the Texas Advanced Computing Center. The authors thank Brian H. Dennis for guidance on mesh generation, Jeiny E. Gutierrez and Thania S. Balcazar for help with the experiments, and Dibesh D. Joshi for assisting with the draft of the paper. The insightful comments of the reviewers are also much appreciated.

References

[1] Goethert, B. H., *Transonic Wind Tunnel Testing*, Dover, Mineola, NY, 2007.

[2] Ludwieg, H., "Tube Wind Tunnel: A Special Type of Blowdown Tunnel," AGARD Rept. R-143, Neuilly sur Seine, France, 1957.

[3] Juhany, K. A., and Darji, A., "Force Measurement in a Ludwieg Tube Tunnel," *Journal of Spacecraft and Rockets*, Vol. 44, No. 1, 2007, pp. 88–93. doi:10.2514/1.21014

[4] Luo, X., Lamanna, G., Holten, A. P. C., and van Dongen, M. E. H., "Effects of Homogeneous Condensation in Compressible Flows: Ludwieg-Tube Experiments and Simulations," *Journal of Fluid Mechanics*, Vol. 572, 2007, pp. 339–366. doi:10.1017/S0022112006003727

[5] Schewe, G., and Steinhoff, C., "Force Measurements on a Circular Cylinder in a Cryogenic Ludwieg-Tube Using Piezoelectric Transducers," *Experiments in Fluids*, Vol. 42, No. 3, 2007, pp. 489–494. doi:10.1007/s00348-007-0250-1

[6] Wolf, T., Estorf, M., and Radespiel, R., "Investigation of the Starting Process in a Ludwieg Tube," *Theoretical and Computational Fluid Dynamics*, Vol. 21, No. 2, 2007, pp. 81–98. doi:10.1007/s00162-006-0040-z

[7] Mouton, C. A., and Hornung, H. G., "Experiments on the Mechanism of Inducing Transition Between Regular and Mach Reflection," *Physics of Fluids*, Vol. 20, No. 12, 2008, Paper 126103. doi:10.1063/1.3042261

[8] Schrijer, F. F. J., and Bannink, W. J., "Description and Flow Assessment of the Delft Hypersonic Ludwieg Tube," *Journal of Spacecraft and Rockets*, Vol. 47, No. 1, 2010, pp. 125–133. doi:10.2514/1.40773

[9] Schülein, E., and Zheltovodov, A., "Effects of Steady Flow Heating by Arc Discharge Upstream of Non-Slender Bodies," *Shock Waves*, Vol. 21, No. 4, 2011, pp. 383–396. doi:10.1007/s00193-011-0307-1

[10] Squire, L. C., "A Review of the Role of Some Small High-Speed Wind Tunnels in Aeronautical Research," *Progress in Aerospace Sciences*, Vol. 34, Nos. 3–4, 1998, pp. 107–166. doi:10.1016/S0376-0421(98)00001-3

[11] Starr, R. F., and Schueler, C. J., "Experimental Studies of a Ludwieg Tube High Reynolds Number Transonic Tunnel," *AIAA Journal*, Vol. 12, No. 3, 1974, pp. 267–268. doi:10.2514/3.49219

[12] Shope, F. L., "Mathematical Model for the Starting Process of a Transonic Ludwieg Tube Wind Tunnel," *Journal of Aircraft*, Vol. 14, No. 6, 1974, pp. 519–520. doi:10.2514/3.58815

[13] Balcazar, T. S., Braun, E. M., Lu, F. K., and Wilson, D. R., "Refurbishment and Testing Techniques in a Transonic Ludwieg Tunnel," *49th AIAA Aerospace Sciences Meeting*, AIAA Paper 2011-1067, Jan. 2011.

[14] Bernstein, L., "Force Measurements in Short Duration Hypersonic Facilities," AGARD, AG-214 Neuilly sur Seine, France, 1975.

[15] Vadassery, P., Joshi, D. D., Rolim, T. C., and Lu, F. K., "Design and Testing of an External Drag Balance for a Hypersonic Shock Tunnel," *Measurement*, Vol. 46, No. 7, 2013, pp. 2110–2117. doi:10.1016/j.measurement.2013.03.011

[16] Joshi, D. D., and Lu, F. K., "Unsteady Thrust Measurement for Pulse Detonation Engines," *Journal of Propulsion and Power*, Vol. 32, No. 1, 2016, pp. 225–236. doi:10.2514/1.B35520

[17] Mee, D. J., "Dynamic Calibration of Force Balances for Impulse Hypersonic Facilities," *Shock Waves*, Vol. 12, No. 6, 2003, pp. 443–455. doi:10.1007/s00193-003-0181-6

[18] Garbaruk, A., Shur, M., Strelets, M., and Spalart, P. R., "Numerical Study of Wind-Tunnel Walls Effects on Transonic Airfoil Flow," *AIAA Journal*, Vol. 41, No. 6, 2003, pp. 1046–1054. doi:10.2514/2.2071

[19] Gardner, A. D., and Richter, K., "Effect of the Model-Sidewall Connection for a Static Airfoil Experiment," *Journal of Aircraft*, Vol. 50, No. 2, 2013, pp. 677–680. doi:10.2514/1.C032011

[20] Oberkampf, W., and Roy, C., *Verification and Validation in Scientific Computing*, Cambridge Univ. Press, Cambridge, MA, 2010.

[21] Peeples, J., "*Experimental Investigation of the Vortex Structure of a Prototype V-22 Blade Tip*," M.S. Thesis, Univ. of Texas at Arlington, Arlington, TX, 1997.

[22] Rath, C., "Wing Tip Vortex Stagnation Pressure Survey of Various Shapes," M.S. Thesis, Univ. of Texas at Arlington, Arlington, TX, 1991.

[23] Kalkhoran, I., "*An Experimental Investigation of the Perpendicular Vortex-Airfoil Interaction at Transonic Speeds*," Ph.D. Thesis, Univ. of Texas at Arlington, Arlington, TX, 1987.

[24] Werling, M. G., Jr., "*Static and Dynamic Calibration of a Multi-Component Sidewall Force Balance for a Transonic Ludwieg Tube*

Wind Tunnel," M.S. Thesis, Univ. of Texas at Arlington, Arlington, TX, 2011.

[25] Pope, A., and Goin, K. L., *High-Speed Wind Tunnel Testing*, Krieger, Malabar, FL, 1978.

[26] Barlow, J. B., Rae, W. H., Jr., and Pope, A., *Low-Speed Wind Tunnel Testing*, Wiley, New York, 1999.

[27] "Recommended Practice. Calibration and Use of Internal Strain-Gage Balances with Application to Wind Tunnel Testing," AIAA Rept. R-091-2003, Reston, VA, 2003.

[28] Sahoo, N., Suryavamshi, K., Reddy, K. P. J., and Mee, D. J., "Dynamic Force Balances for Short-Duration Hypersonic Testing Facilities," *Experiments in Fluids*, Vol. 38, No. 5, 2005, pp. 606–614. doi:10.1007/s00348-005-0932-5

[29] Kolsky, H., *Stress Waves in Solids*, Dover, Mineola, NY, 1963.

[30] Robinson, M., "*Simultaneous Lift, Moment and Thrust Measurements on a Scramjet in Hypervelocity Flow*, " Ph.D. Thesis, Univ. of Queensland, Brisbane, Australia, 2003.

[31] Biedron, R. T., Derlaga, J. M., Gnoffo, P. A., Hammond, D. P., Jones, W. T., Kleb, B., Lee-Rausch, E. M., Nielsen, E. J., Park, M. A., Rumsey, C. L., Thomas, J. L., and Wood, W. A., "*FUN3D Manual: 12.4*, " NASA TM-2014-218179, 2014.

[32] Nambu, T., Hashimoto, A., Ueno, M., Murakami, K., and Sato, T., "Evaluation of Wall-Interference Correction Method Using Numerical Analysis and Porous Wall Model," *Journal of Aircraft*, Vol. 52, No. 1, 2015, pp. 226–234. doi:10.2514/1.C032675

[33] Marcum, D. L., and Weatherhill, N. P., "Unstructured Grid Generation Using Iterative Point Insertion and Local Reconnection," *AIAA Journal*, Vol. 33, No. 9, 1995, pp. 1619–1625. doi:10.2514/3.12701

[34] Marcum, D. L., *Unstructured Grid Generation Using Automatic Point Insertion and Local Reconnection*, CRC Press, Boca Raton, FL, 1998.

[35] Bibb, K., Gnoffo, P., Park, M., and Jones, W., "Parallel, Gradient-Based Anisotropic Mesh Adaptation for Re-Entry Vehicle Configurations," *9th AIAA/ASME Joint Thermophysics and Heat Transfer Conference, Fluid Dynamics and Co-Located Conferences*, AIAA Paper 2006-3579, 2006. doi:10.2514/6.2006-3579

[36] Shenoy, R., Smith, M. J., and Park, M. A., "Unstructured Overset Mesh Adaptation with Turbulence Modeling for Unsteady Aerodynamic Interactions," *Journal of Aircraft*, Vol. 51, No. 1, 2014, pp. 161–174. doi:10.2514/1.C032195

[37] Mineck, R. E., and Hartwich, P. M., "Effect of Full-Chord Porosity on Aerodynamic Characteristics of the NACA 0012 Airfoil," NASA TP-3591, 1996.

[38] Harris, C. D., "Two-Dimensional Aerodynamic Characteristics of the NACA 0012 Airfoil in the Langley 8-Foot Transonic Pressure Tunnel," NASA TM-81927, 1981.